

Wettability-Engineered Meshes for Gas Microvolume Precision Handling in Liquids

*Original*

Wettability-Engineered Meshes for Gas Microvolume Precision Handling in Liquids / Bernardini, Jacopo; Sen, Uddalok; Jafari Gukeh, Mohamad; Asinari, Pietro; Megaridis, Constantine M. - In: ACS APPLIED MATERIALS & INTERFACES. - ISSN 1944-8244. - ELETTRONICO. - 12:15(2020), pp. 18046-18055-18055. [10.1021/acsami.9b22284]

*Availability:*

This version is available at: 11583/2814192 since: 2020-04-21T09:22:16Z

*Publisher:*

American Chemical Society

*Published*

DOI:10.1021/acsami.9b22284

*Terms of use:*

This article is made available under terms and conditions as specified in the corresponding bibliographic description in the repository

*Publisher copyright*

ACS postprint/Author's Accepted Manuscript

This document is the Accepted Manuscript version of a Published Work that appeared in final form in ACS APPLIED MATERIALS & INTERFACES, copyright © American Chemical Society after peer review and technical editing by the publisher. To access the final edited and published work see <http://dx.doi.org/10.1021/acsami.9b22284>.

(Article begins on next page)

# Wettability-Engineered Meshes for Gas Micro-Volume Precision Handling in Liquids

Jacopo Bernardini,<sup>†,‡</sup> Uddalok Sen,<sup>†</sup> Mohamad Jafari Gukeh,<sup>†</sup> Pietro Asinari,<sup>‡</sup> and Constantine M. Megaridis<sup>\*,†</sup>

<sup>†</sup>*Department of Mechanical and Industrial Engineering, University of Illinois at Chicago, Chicago, IL 60607, USA*

<sup>‡</sup>*Department of Energy, Politecnico di Torino, Corso Duca degli Abruzzi 24, Torino, Italy*

E-mail: cmm@uic.edu

## Abstract

The interaction of rising gas bubbles with submerged air-repelling or air-attracting surfaces is relevant to various technological applications that rely on gas micro-volume handling or removal. This work demonstrates how submerged metal meshes with super air-attracting/repelling properties can be employed to manipulate micro-volumes of air, rising buoyantly in the form of bubbles in water. Super-aerophobic meshes are observed to selectively allow the passage of air bubbles depending on the mesh pore size, the bubble volume-equivalent diameter, and the bubble impact velocity on the mesh. Differently, super-aerophilic meshes reduce or amplify the volume captured from a train of incoming bubbles. Finally, a wettability spatial pattern on the mesh is used to control the size of the outgoing bubble, and an empirical relation is formulated to predict the released volume. The study demonstrates how porous materials with controlled wettability can be used to precisely modulate and control the outcome of bubble/mesh interactions.

## Introduction

The wettability of a solid surface is the property that determines the behavior of a liquid volume coming in contact with the solid; this property has been the subject of exten-

sive research over many decades.<sup>1–4</sup> In attempts to biomimic organic surfaces,<sup>5</sup> such as the lotus leaf (which possesses super water-repelling properties), many techniques have been developed to produce superhydrophobic (water-repelling) and superhydrophilic (water-attracting) substrates.<sup>6–9</sup> Only in the last couple of decades, attention has been shifted to the complementary scenario where a rising gas bubble encounters a submerged solid substrate, and thus the concept of air-repelling and air-attracting properties has emerged.<sup>10–17</sup> A hydrophilic surface is aerophobic when under water, and vice versa for a hydrophobic surface.<sup>18</sup> The equilibrium contact angles of a liquid drop on a solid substrate and an air bubble on the same submerged (underwater) solid substrate are supplementary. A literature review on submerged aerophobic and aerophilic substrates by George et al.<sup>18</sup> highlighted the characteristics and applications of these surfaces. The interaction between gas bubbles and underwater metal meshes with controlled wettability was recently considered for underwater bubble transportation. Pei et al.<sup>19</sup> employed integrated Janus meshes to promote bubble unidirectional penetration underwater (bubble diode). However, no prior work has focused on utilising submerged permeable meshes with controlled wettability to manipulate the volume of gas micro-bubbles rising buoyantly in viscous fluids. Such processes are important when precise handling

of bubbles is required (e.g. for catalysis or sensing), or when gas bubbles must be captured and removed (e.g. fuel tanks, waste water remediation).

Meshes exhibiting super-aerophobic or super-aerophilic behaviors, or their combinations, are important for the multiple applications they may find in two-phase flow systems. Such flows, frequently involving both liquid and gas (bubbles) phases, are used in bubble column reactors<sup>20,21</sup> in the chemical industry. The volume fraction of the gas, bubble size, and interfacial area are important design parameters that govern the proper operation of the reactor.<sup>22,23</sup> Solid meshes that have different responses when interacting with small gas volumes could consequently find applications as sensors or as means to control and influence the bubble volume, shape, and size in different segments of a reactor. On the other hand, the presence of gas bubbles could be undesirable, or even dangerous, in applications involving oil for fluid power systems.<sup>24</sup> In this and other similar cases, the meshes could be employed as efficient and economical gas filters. Other potential applications of meshes exhibiting air-attracting/repelling properties could be in the biomedical industry, where gas bubbles need to be separated from biological fluids, such as blood,<sup>25</sup> or in drug delivery applications.<sup>26</sup> Given the acute shortage of literature in this domain, the aforementioned potential applications serve as motivation for the present work.

In the present study, we demonstrate the applicability of wettability-patterned, metal meshes to manipulate the size of gas bubbles rising through a viscous fluid. The interaction of rising gas bubbles with uniformly super-aerophilic and super-aerophobic meshes is studied first, followed by bubble interaction with two vertically-stacked meshes of uniform wettability. Finally, the use of wettability-patterned meshes for controlling released-bubble size is presented as an example of what could be achieved with this method, which, of course, is not limited to just water and air, but could be adapted for other liquid/gas pairs, as long as repellency to these other liquids can be attained.

## Materials and methods

Woven wire meshes of aluminum are used (McMaster-Carr<sup>®</sup>) in the present work. These meshes are defined by their opening size ( $w$ ) and wire diameter ( $b$ ) (see Fig. 1 A). Each mesh is characterized by a number, which indicates the number of pores per inch of the mesh. The meshes used in this study, along with their salient dimensions, are listed in Table 1.

Table 1: Salient geometric dimensions (see Fig. 1) of the meshes used in the experiments

Mesh	$w$ (mm)	$b$ (mm)
M10	1.905	0.635
M12	1.524	0.584
M14	1.295	0.508
M16	1.143	0.457
M20	0.864	0.406
M30	0.559	0.279

Aluminum is an intrinsically-hydrophilic material due to its high surface energy. One method to make aluminum superhydrophilic (i.e. super-aerophobic) consists of acid etching (ACS reagent 37%, Sigma-Aldrich<sup>®</sup>), followed by boiling in deionized water,<sup>27</sup> as shown in steps B1 and B2 of Fig. 1. After drying in an oven (Fig. 1 B3), the mesh is immersed in a 1% wt 1H,1H,2H,2H-perfluorodecyltriethoxysilane [97%, Sigma-Aldrich<sup>®</sup>, fluoro-alkyl silane(FAS)] in ethanol (200 proof, Decon Labs<sup>®</sup>) solution (Fig. 1 B4), so that a thin layer of FAS is formed on the surface of the mesh wires, making the mesh super-aerophilic. At the end of the treatment shown in Fig. 1 B1-B4, the mesh has become uniformly super-aerophilic. A wettability pattern consisting of spatially juxtaposed super-aerophobic and super-aerophilic regions can be obtained through selective laser etching (Fig. 1 B6). A CAD file representing the mesh pattern (Fig. 1 B5) is used as a vector image for a laser marking system (EMS400, TYKMA Electrox<sup>®</sup>, 30% power, 50 kHz intensity, and 200 mm/s traverse speed). The laser selectively ablates the FAS coating from the mesh wires, rendering them super-aerophobic. The mesh is then placed on an aluminum support (Fig. 1

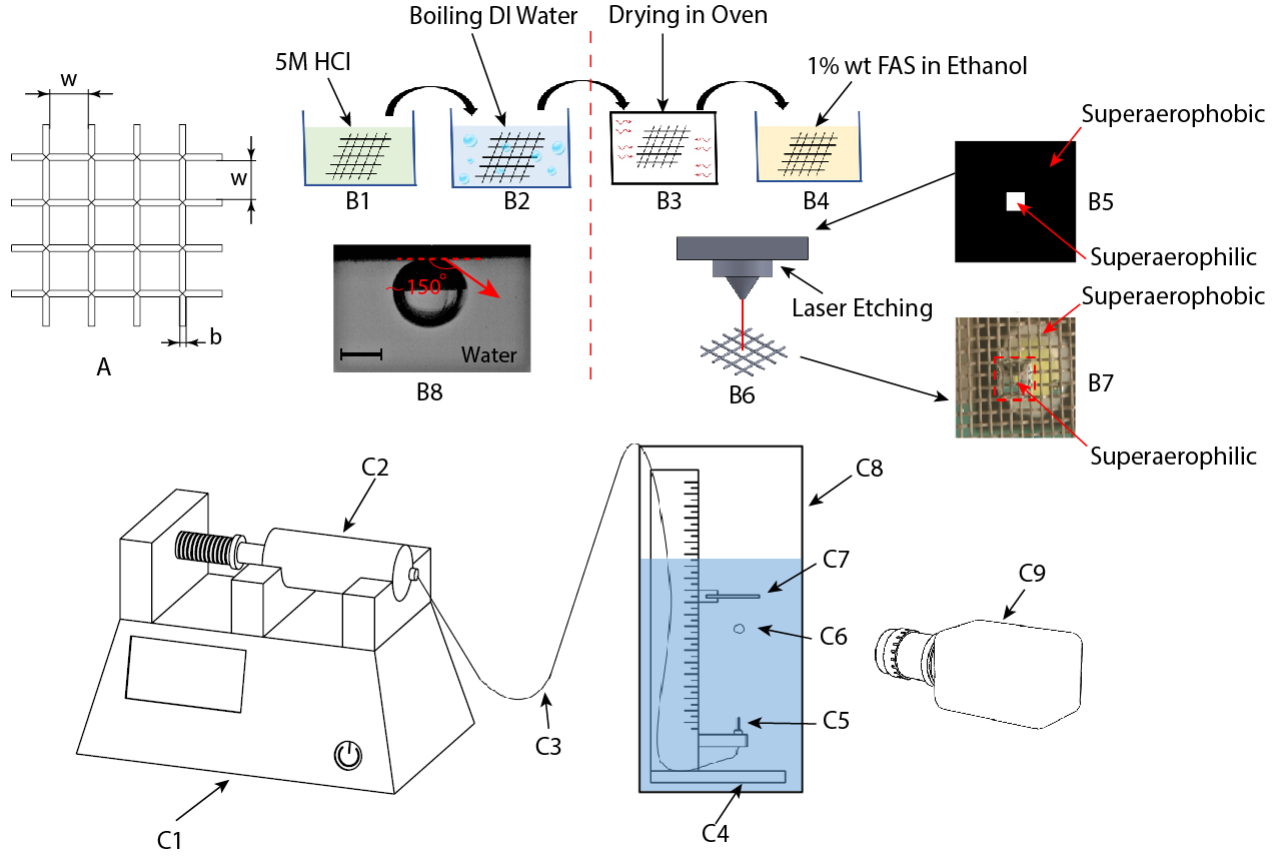


Figure 1: A: Mesh top view showing the characteristic opening size,  $w$ , and wire diameter,  $b$ . B1: the mesh is first submerged in 5M HCl solution for an interval between 12 and 20 minutes; B2: the mesh is passivated in boiling deionized water for 60 minutes. After steps B1 and B2, the mesh has become super-aerophobic; the equilibrium contact angle measured for a bubble resting on a submerged flat aluminum substrate treated in such way is  $\theta_e = 149^\circ \pm 2.3^\circ$ . B3: the mesh is dried in an oven at  $40^\circ\text{C}$  for 40 minutes; B4: the mesh is immersed in 1% wt FAS in ethanol solution for 8-10 hours. After step B4, the mesh has become super-aerophilic. B5: CAD pattern used as vector image for the laser marking system; the black region is the one etched by the laser, the white region is masked and thus unaffected by the laser. B6: laser marking procedure. B7: effective result of the laser marking process on a M20 mesh. The region confined in the red dashed line is super-aerophilic, the surrounding region is super-aerophobic. C1-C9: complete set-up for bubble generation and data collection. C1: syringe pump; C2: 10 mL plastic syringe; C3: clear tube; C4: aluminum support; C5: dispensing needle; C6: rising bubble; C7: mesh held in mesh holder; C8: rectangular transparent glass tank; C9: high-speed camera.

C4), and inserted in a rectangular transparent glass tank (Fig. 1 C8), filled with DI water up to the desired level. The aluminum support allows the vertical alignment of the mesh (Fig. 1 C7) with a dispensing needle (Fig. 1 C5, Precision Tips, Nordson EFD®). The needle is connected through a clear tube (Fig. 1 C3) to a plastic syringe (Fig. 1 C2), which is mounted on a syringe infusion pump (Fig. 1 C1, PHD ULTRA, Harvard Apparatus®). The pump is used to dispense air bubbles (Fig. 1 C6), which rise with terminal velocity soon after dispensing,<sup>28–33</sup> and reach the bottom surface of the mesh. The mesh is placed at a vertical distance from the needle such that the bubble reaches its terminal velocity along a linear trajectory,<sup>34</sup> which is critical to have always the same bubble on mesh point of impact. The interaction between the air bubble and the mesh is recorded with a high-speed digital camera (Fig. 1 C9, Phantom Miro 310, Vision Research AMETEK®), and each frame of the video is then analyzed with the Image Processing Toolbox of MATLAB®.

## Results and discussion

The continuous phase is DI water at 25°C and atmospheric pressure, while the dispersed phase is air. Air bubbles of three different sizes were generated ( $d_{eq} = 1.86, 2.90, \text{ and } 3.90 \text{ mm}$ ), as desired, in the present experiments. Because of bubble deviations from the spherical shape, volume-equivalent diameters were determined with MATLAB® using the video frames captured with the high-speed camera. Firstly, the algorithm designated the air-water interface as the sharp discontinuity in the image intensity. Next, the bubble contour was filled, and the image was binarized (the grey-scale image was transformed into a black and white image). Finally, given the axisymmetric shape, the bubble volume was calculated as that of a surface of revolution. The dimensionless Morton and Bond numbers are, respectively,  $Mo = \frac{g\mu_l^4(\rho_l - \rho_g)}{\sigma^3\rho_l^2} = 1.73 \times 10^{-11}$  and  $0.47 < Bo = \frac{g(\rho_l - \rho_g)d_{eq}^2}{\sigma} < 2.07$ . In the expressions for Bo and Mo,  $\rho_l$  and  $\rho_g$  are, re-

spectively, the liquid and gas phase densities,  $\mu_l$  the liquid dynamic viscosity,  $g$  the gravitational acceleration,  $d_{eq}$  the bubble volume-equivalent diameter, and  $\sigma$  the liquid-gas interface tension. Given these values of  $Bo$  and  $Mo$ , each bubble can be classified into the ellipsoidal regime,<sup>28</sup> meaning that the surface tension forces are prevailing and the shape of the bubble is oblate. The experimental terminal velocities,  $v_t$ , range in the interval  $0.3 < v_t < 0.36 \text{ m/s}$ , corresponding to  $740 < Re < 1300$ , with  $Re$  being the Reynolds number ( $Re = \frac{\rho_l v_t d_{eq}}{\mu_l}$ ). The experimental  $Re$  is congruent with values in the literature for air bubbles of similar size rising in DI water.<sup>28,29</sup> Hereafter, different configurations are analyzed: uniformly super-aerophobic and super-aerophilic single meshes, series of vertically-stacked meshes with uniform wettability, and wettability-patterned meshes. In each case, the mesh is placed at a vertical distance of 2 cm from the tip of the dispensing needle (so that terminal velocity is attained before impact).

## Gas bubble interacting with super-aerophobic mesh

When an air bubble, which rises buoyantly at terminal velocity, encounters a super-aerophobic mesh, two different outcomes can be observed, depending on the relative values of  $w$  and  $d_{eq}$ , as shown in Video S1 of the Supporting Information. If the ratio  $d_{eq}/w$  is low, the bubble can squeeze and penetrate through a single pore of the mesh. For high  $d_{eq}/w$ , the bubble bounces on the under-side of the mesh and stays there after a short transient. The opening size of the mesh plays an important role in bubble-passage behavior. Small opening leads to bouncing and keeping the bubble beneath the mesh.<sup>35–37</sup> The critical ratio  $d_{eq}/w$  for passage was found to lay between 1.63 and 1.84 in the present work. So if  $d_{eq}/w < 1.63$ , a bubble rising at terminal velocity is likely to penetrate the mesh. Differently, if  $d_{eq}/w > 1.84$ , the bubble would bounce on the under-side of the mesh and stay there. Upon impact, just at the moment when the upper gas-liquid interface curvature has reached its maximum,

the gas volume is assumed to have attained the shape approximated by two hemispheres, as shown in Fig. 2. The hemisphere at the top has a diameter  $w$ , corresponding to the mesh opening size. This assumption is supported by the super-aerophobicity of the mesh wires. The hemisphere at the bottom has a diameter  $D$ , which is determined by the volume conservation of the air bubble during impact. The volume conservation can be enforced because compressibility effects are negligible for the terminal velocity ( $v_t \leq 0.36$  m/s, Mach number  $Ma < 2.4 \cdot 10^{-4}$ ) of these gas bubbles.<sup>38</sup> For an air bubble interacting with a single pore of the mesh,  $D$  is determined from

$$D = (2d_{eq}^3 - w^3)^{\frac{1}{3}} \quad (1)$$

When the gas-liquid interface is convex, the pressure inside the bubble is higher than the pressure in the surrounding liquid, as the Young-Laplace equation predicts.<sup>4</sup> The pressure difference across the gas-liquid interface can be determined by  $\Delta P = -\sigma \nabla \cdot \hat{n}$ , where  $\hat{n}$  is the outward unit vector normal to the interface (from gas to liquid side), and consequently,  $\nabla \cdot \hat{n}$  is the local interface curvature. At the moment shown in Fig. 2b, the gas-liquid interface curvature causes an increased gas pressure in the top hemisphere, which resists further buildup in gas volume, thus hindering the passage of the bubble through a mesh gap. The maximum capillary anti-penetration pressure,<sup>39–42</sup>  $\Delta P_{ap}$ , can be estimated as

$$\Delta P_{ap} \simeq -\frac{4\sigma}{w} \cos \theta_c = P_{up} - P_0 \quad (2)$$

where  $P_{up}$  is the gas pressure at the upper interface,  $P_0$  the liquid pressure at the same interface (reference pressure), and  $\theta_c$  the equilibrium contact angle, which was measured to be  $\theta_c \simeq 150^\circ$  (see Fig. 1 B8). In our experiments, we found  $195 \text{ Pa} < \Delta P_{ap} < 293 \text{ Pa}$  for the different mesh sizes.

In order for the bubble to penetrate the mesh, the gas pressure at the lower side of the gas-liquid interface,  $P_{lo}$ , must overcome the gas pressure at the upper side,  $P_{up}$  (see Fig. 2b). From the lower side, there are several contri-

butions to pressure that help the bubble pass through the mesh gap. The Young-Laplace pressure at the lower side of the bubble can be written as  $\Delta P_{lo} = \frac{4\sigma}{D}$ . Considering the hydrostatic pressure difference due to the height of the bubble, we can add  $P_{hs} = \rho(\frac{D}{2} + \frac{w}{2})g$  on the lower-side pressure. In addition, the pressure due to the buoyancy is  $P_B = F_B/w^2$ , where the buoyancy force  $F_B = \frac{\pi}{6}d_{eq}^3(\rho_l - \rho_g)g$ . Most importantly, we experimentally observed that penetration does not occur when the same bubble reaches the same mesh with a velocity lower than its terminal one, as shown in Fig. 3. Therefore, inertia plays a critical role in determining bubble penetration (or not) after impact on the super-aerophobic mesh. Numerous numerical and experimental studies in the literature have investigated the dynamics of a single bubble rising in a viscous fluid and the flow structure surrounding the bubble.<sup>43–45</sup> During the buoyant ascent, the liquid in front of the bubble nose is pushed upward, while the fluid behind the bubble is pulled up by the wake.<sup>46</sup> The velocity magnitude of the liquid behind the bubble is reportedly almost equal to the bubble velocity itself. Consequently, the bubble velocity can be used to estimate the liquid dynamic pressure at the moment of the impact, namely  $P_d \simeq \frac{1}{2}\rho_l v^2$ ,<sup>47,48</sup> where  $v$  is the bubble impact velocity on the mesh. Therefore, the composite pressure on the lower side of the deformed bubble (Fig. 2b) is

$$P_{lo} \simeq P_0 + \Delta P_{lo} + P_{hs} + P_B + P_d \quad (3)$$

In the present experiments, we found that  $185 \text{ Pa} < P_{lo} - P_0 < 252 \text{ Pa}$ , based on various mesh sizes and bubble impact velocities. These experiments were performed after ensuring central impact of the bubble on the mesh by way of an x-y micro-positioning stage mounted in the horizontal plane to align the bubble impact with the mesh opening. With this system, the impact point did not change, thus ensuring reproducibility of the results. For an air bubble with  $d_{eq} = 1.86 \text{ mm}$ , rising in water with terminal velocity ( $v_t = 0.36 \text{ m/s}$ ) and impacting a super-aerophobic M16 mesh ( $w = 1.143 \text{ mm}$ ), penetration was experimentally observed. For

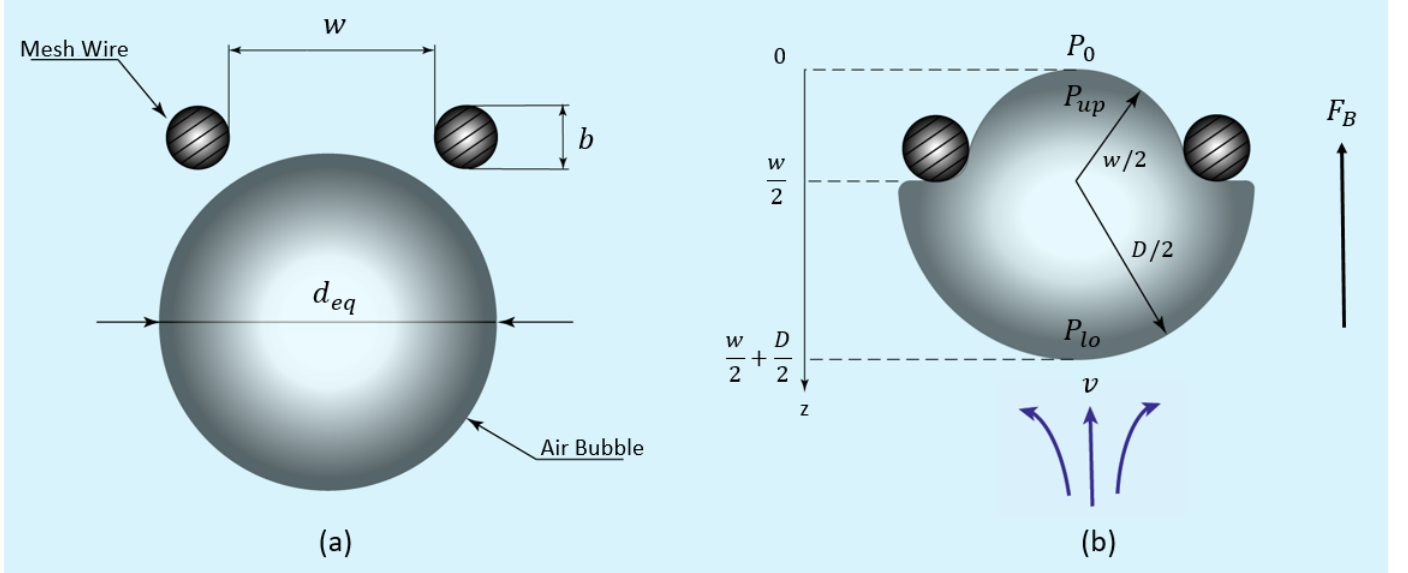


Figure 2: (a) Schematic showing an air bubble with volume equivalent diameter  $d_{eq}$  just before it impacts centrally on a mesh opening; the mesh wires have a diameter  $b$  and are spaced apart by  $w$ . (b) Schematic of the air bubble as the curvature of upper gas-liquid interface has reached its maximum. The volume of the bubble consists of two hemispheres; the one at the top has a diameter  $w$ , and the one at the bottom has a diameter  $D$ . The liquid trailing the bubble is induced to motion after the gas passes. The bubble curvatures around the wires are exaggerated and are not expected to occur in practice.

such a bubble-mesh combination,  $P_{up} - P_0 \simeq 222$  Pa, while  $P_{lo} - P_0 \simeq 237$  Pa. Consequently,  $P_{lo} > P_{up}$ , which explains the penetration outcome. When the impact velocity of the same bubble on the same mesh was decreased to 0.30 m/s, which was accomplished by decreasing the distance separating the dispensing needle from the mesh, the lower side pressure was reduced to  $P_{lo} - P_0 \simeq 216$  Pa. In this case,  $P_{lo} < P_{up}$ , and the bubble did not penetrate the mesh. Separately, when an identical air bubble hit a super-aerophobic M14 ( $w = 1.29$  mm) mesh at terminal velocity, the pressure at the upper interface  $P_{up} - P_0 \simeq 195$  Pa, while  $P_{lo} - P_0 \simeq 234$  Pa, so the bubble penetrated the mesh. Finally, when the impact velocity of that bubble was reduced to  $v = 0.18$  m/s, the lower-side pressure became  $P_{lo} - P_0 \simeq 185$  Pa, with the bubble remaining on the mesh underside. Furthermore, bubble penetration was never observed for meshes having a gap size  $w \leq 0.864$  mm, which corresponds to  $P_{up} - P_0 \geq 293$  Pa.

## Gas bubble interacting with super-aerophilic mesh

Two different experimental approaches may be adopted for investigating the bubble-mesh interaction with uniformly super-aerophilic meshes. In the first approach, the mesh is submerged into DI water and an air film is left intact between the mesh wires; in this case the mesh is conveniently defined as ‘dried’. In the second approach, the mesh is submerged into DI water and the air is then removed from the mesh gaps by withdrawing it with a syringe. This way, the air is trapped only inside the surface roughness features of the wires. In this case, the mesh is conveniently defined as ‘wet’, meaning that water occupies the mesh gaps. In the wet case, right after the impact of the air bubble on the bottom side of the mesh, the air is able to penetrate the mesh and a pendant bubble is formed on the top surface of the mesh. The bubble stays pinned on the top surface in equilibrium, under the combined effects of buoyancy and capillarity (differently from the super-aerophobic case, as shown in



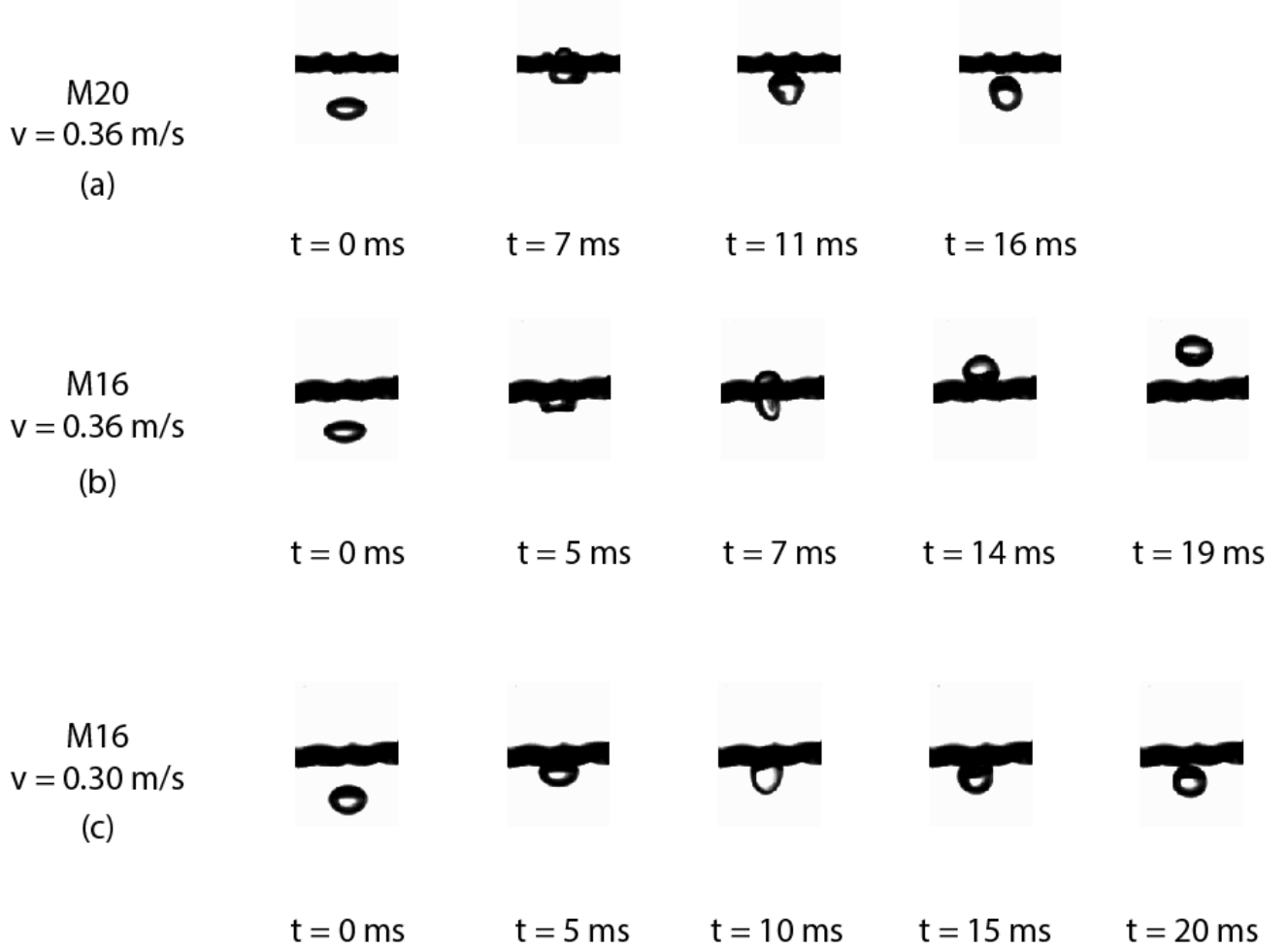


Figure 3: Time-lapsed images showing the central impact of an air bubble with  $d_{eq} = 1.86$  mm on (a) a super-aerophobic M20 mesh ( $w = 0.86$  mm) with an impact velocity  $v = 0.36$  m/s (terminal velocity), (b) a super-aerophobic M16 mesh ( $w = 1.14$  mm) with the same impact velocity, and (c) a super-aerophobic M16 mesh with a lower impact velocity  $v = 0.30$  m/s. In (a) and (c) the bubble cannot penetrate the mesh. In (b), the air volume gets squeezed, and the bubble penetrates through a mesh opening. The different outcome in (b) and (c) emphasizes the importance of the bubble's impact velocity.



Fig. 3a). The magnitude of the capillary force,  $F_C$ , can be calculated by

$$|\vec{F}_C| = \sigma p \quad (4)$$

where  $p$  is the dried perimeter.

The buoyancy force acts in the upward direction and causes the lighter air to rise in the denser water. On the other hand, capillarity acts downward, as it retains the air on the mesh wires due the lower energy state associated with the gas-solid interface as compared to the gas-liquid interface. As more and more incoming (IC) bubbles impact the mesh, the pendant bubble keeps growing until the balance between buoyancy and capillarity is broken. At this point, bubble pinch-off occurs (as shown in Video S2 of the Supporting Information), and an outgoing (OG) bubble detaches from the mesh (Fig. 4). On the other hand, in the dried case, the bubble disappears after reaching the mesh, due to the fact that the air bubble volume merges with the trapped air within the mesh gaps. The formation of a pendant bubble can be observed only after a significant amount of air has been trapped in the mesh. It is noted that the experimental results presented hereafter are all for the wet mesh case.

The volume of the outgoing bubble,  $V_{OG}$ , detaching from the super-aerophilic mesh is dependent both on the volume of each incoming bubble,  $V_{IC}$ , and on the pore size of the uniform super-aerophilic mesh,  $w$ . These effects have been investigated by measuring the OG bubble volumes resulting from different combinations of meshes and incoming bubble volumes. Four different meshes were used: M12, M16, M20, and M30. For each possible combination of mesh size and volume of the incoming bubble,  $V_{OG}$  was measured. A volume amplification factor, AF, was then determined by  $V_{OG}/V_{IC}$ .  $V_{OG}$  is strongly dependent on the volume of air that the mesh is able to retain before the departure of the OG bubble. Meshes having different gap size are able to trap different volumes of air, and thus the OG bubble volume varies by mesh. The obtained results are summarized in Fig. 5.

From Fig. 5a, the bigger the volume of a single incoming bubble, the larger the OG bubble

volume. This is attributed to two reasons. If  $V_{thr}$  is the threshold gas volume for which buoyancy and capillary forces are balanced, then  $V_{OG} \approx V_{thr} + V_{IC} - \Delta V$ ,  $V_{IC}$  being the volume of the last incoming bubble before the OG bubble departs, and  $\Delta V$  the volume of air trapped in the mesh after the pinch-off. Naturally, the larger  $V_{IC}$  is, the bigger is the size of the OG bubble. In addition,  $V_{thr}$  itself depends on  $V_{IC}$ : larger IC bubbles dry more mesh gaps, creating a greater dried perimeter, i.e. higher  $F_C$ . The larger  $F_C$  causes an increment in  $V_{thr}$  needed for  $F_B$  to overcome  $F_C$ . As far as  $\Delta V$  is concerned, it depends both on the dried perimeter and the mesh pore-size – finer meshes are likely to be able to retain a larger amount of air volume due to the higher solid-gas interface available. Furthermore, it was observed that, especially for small  $V_{IC}$ , finer meshes with a smaller gap size produced a bigger OG bubble. This is caused by the strong dependence of  $V_{OG}$  on the volume of air, or number of IC bubbles, that can be retained by the mesh before the detachment of the OG bubble. Finer meshes make the horizontal spreading of air easier, due to the larger solid surface area available, as compared to coarser meshes. This results in a larger dried perimeter, which, in turn, enhances the capillary force  $F_C$ . As already discussed, an enhancement in  $F_C$  causes a larger  $V_{thr}$ , and thus a larger  $V_{OG}$ . Consequently, while finer meshes retain a bigger  $\Delta V$ , resulting in a smaller  $V_{OG}$ , they also allow a larger dried perimeter, which raises the value of  $V_{OG}$ . The experimental evidence shows that the latter effect prevails over the former, since  $V_{OG}$  is found to increase with declining mesh pore-size.

From Fig. 5b, when bubbles with  $d_{eq} = 1.86$  mm ( $V_{IC} = 3.37\mu L$ ) and  $d_{eq} = 2.90$  mm ( $V_{IC} = 12.77\mu L$ ) impact a super-aerophilic mesh, the amplification factor tends to decrease for larger mesh gaps ( $w$ ). But for bubbles with  $d_{eq} = 3.9$  mm ( $V_{IC} = 31.06\mu L$ ), the amplification factor changes little for different mesh gaps. This result may be explained by noting again that  $V_{OG} \approx V_{thr} + V_{IC} - \Delta V$ . For the largest incoming bubbles, the changes in  $V_{OG}$ , and consequently in AF, resulting from different meshes may be comparable with the value of  $V_{IC}$  itself.

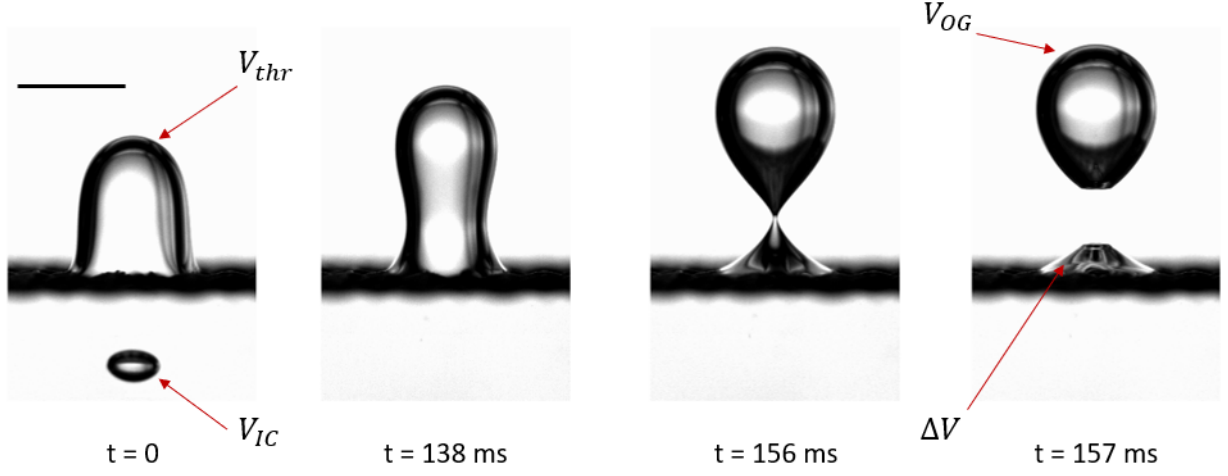


Figure 4: Time-lapsed images showing an air bubble in equilibrium on the top surface of a super-aerophilic M20 ( $w = 0.86$  mm) mesh after a stream of incoming bubbles of  $d_{eq} = 1.86$  mm impacted the mesh. Once the equilibrium is disrupted, a gradually-thinning neck is formed. After the neck radius reaches a minimum, bubble pinch-off occurs.  $V_{IC}$  is the volume of a single incoming (i.e. IC) bubble,  $V_{thr}$  is the volume of the largest pendant bubble in equilibrium on the upper side of the mesh,  $V_{OG}$  is the volume of the outgoing (i.e. OG) bubble, and  $\Delta V$  is the volume of air remained trapped within the mesh wires after pinch-off. The scale bar denotes 5 mm.

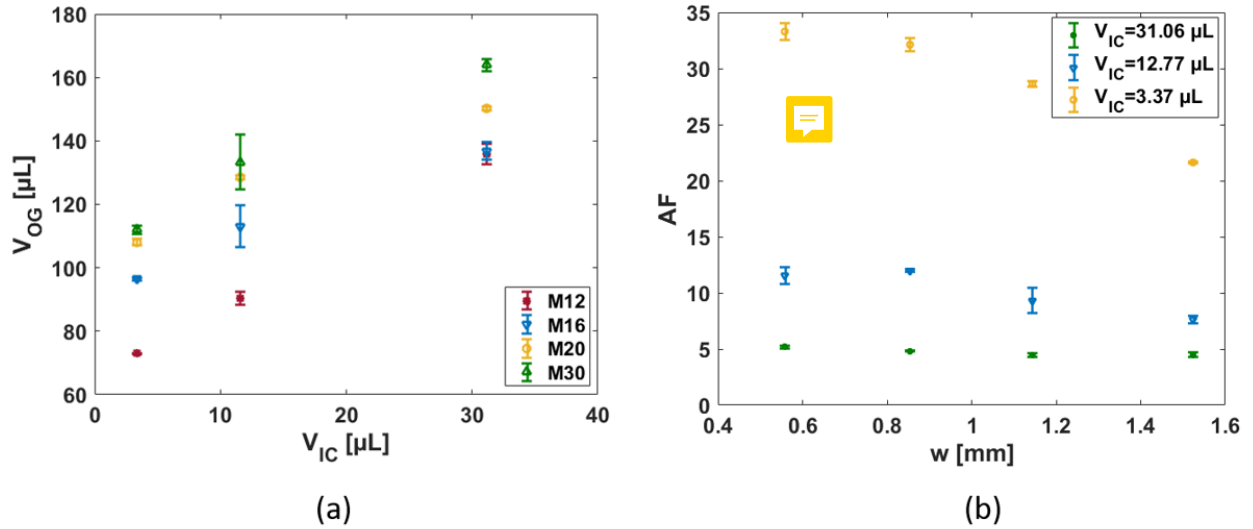


Figure 5: Variation of (a) outgoing (OG) bubble volume with each incoming (IC) bubble volume for different meshes: M12 ( $w = 1.52$  mm), M16 ( $w = 1.14$  mm), and M20 ( $w = 0.86$  mm). (b) Amplification Factor, AF, vs. mesh opening size,  $w$ , for different incoming bubble volumes.

Thus, for high  $V_{IC}$  values, changes in AF for different meshes cannot be resolved adequately.

## Gas bubbles interacting with two vertically-stacked meshes of uniform wettability

The maximum amplification factor obtained with a single, uniformly super-aerophilic mesh was  $AF_{max} \approx 34$ . This result was obtained with a super-aerophilic mesh M30 ( $w = 0.56$  mm) and IC bubbles of  $d_{eq} = 1.86$  mm. An even stronger amplification factor can be obtained by placing two super-aerophilic meshes in series, one on top of the other, with a vertical gap in between, so that the OG bubble from the first mesh can encounter the second one. As shown in Video S3 of the supporting information for the M30-M20 combination, as soon as a second IC bubble coming from the mesh at the bottom ( $V_{IC} \simeq 107$   $\mu$ L in Video S3) hits the top mesh, a single OG bubble detaches from the second mesh with a volume that is much bigger than the volume of a single IC bubble ( $V_{OG} \simeq 204$   $\mu$ L in Video S3). Differently, a pair of vertically-stacked super-aerophilic meshes may also be employed to first amplify (bottom mesh) and then reduce (mesh on top) the volume of an IC bubble (see Video S3, M8-M30 combination, of the supporting information). This is accomplished by placing a coarser mesh on top of a finer one. The mesh on top is not able to retain the whole volume of air rising from the bottom mesh. Consequently, only a fraction of the bubble volume coming from the bottom mesh is trapped within the second mesh, while the remaining volume of air continues rising. Furthermore, if a uniformly super-aerophobic mesh is placed on top of a uniformly super-aerophilic mesh, it is possible to trap the bubble resulting from the first mesh in the vertical gap between the two meshes. The volume of the trapped bubble is determined by the opening size of the mesh on the bottom and by the size of the IC bubbles. The three different possible behaviors are shown in Fig. 6.

Different combinations of super-aerophilic meshes are considered, and for each combi-

nation, the volume of the bubble detaching from the top mesh is measured, allowing to calculate the amplification factor, AF, in each case. Figure 7 shows the results for different combinations of super-aerophilic meshes. For all cases in Fig. 7, the experiments revealed that except for the M20-M12 and M16-M10 combinations,  $AF > AF_{max,1} = 34$ , where  $AF_{max,1}$  is the maximum amplification factor obtained with a single super-aerophilic mesh. With the exception of the M20-M12 and M16-M10 combinations (see Fig. 7), there are three distinct levels of AF values:  $70 \lesssim AF \lesssim 80$ ,  $50 \lesssim AF \lesssim 60$ , and  $40 \lesssim AF \lesssim 50$ . Each range can be easily associated with the pore size of the mesh placed at the bottom. The highest AF range is obtained with a M20 mesh at the bottom ( $w = 0.86$  mm), while the lowest range results from placing a M12 mesh ( $w = 1.52$  mm) at the bottom. Therefore, as far as the mesh on top is capable of capturing the entire incoming bubble volume, the AF correlates with the pore size of the bottom mesh: the finer the mesh, the higher the AF. This result could be predicted from Fig. 5b, which shows that for larger IC bubbles ( $V_{IC} = 31.06$   $\mu$ L),  $V_{OG}$  does not change significantly by employing meshes of different  $w$ . In case of two meshes in series, the smallest bubble resulting from the bottom mesh is  $d_{eq} \approx 6$  mm, and thus the influence of the top mesh is likely to be negligible (under the limit that the bubble can be captured by the mesh). The highest amplification factor observed in the present experiments by placing two super-aerophilic meshes in series is  $AF_{max} \approx 78$  (i.e.  $V_{OG} \approx 263$   $\mu$ L).

The bubble-volume reduction effect in Fig. 7 was investigated further by placing M8 ( $w = 2.46$  mm), M10 ( $w = 1.90$  mm) and M12 ( $w = 1.52$  mm) super-aerophilic meshes above the M20 ( $w = 0.86$  mm) super-aerophilic mesh. In all cases, the IC bubble volume was  $V_{IC} \approx 31$   $\mu$ L. The volume of the bubble released from the M20 mesh was  $V_{M20} \approx 145.7 \pm 2.15$   $\mu$ L. For all three cases, the top mesh was not able to retain the whole amount of air rising from the underlying M20 mesh. The gas volume trapped in the top mesh after pinch-off was  $\Delta V_{series} = V_{M20} - V_{OG}$ , where  $V_{OG}$  is the volume of the out-

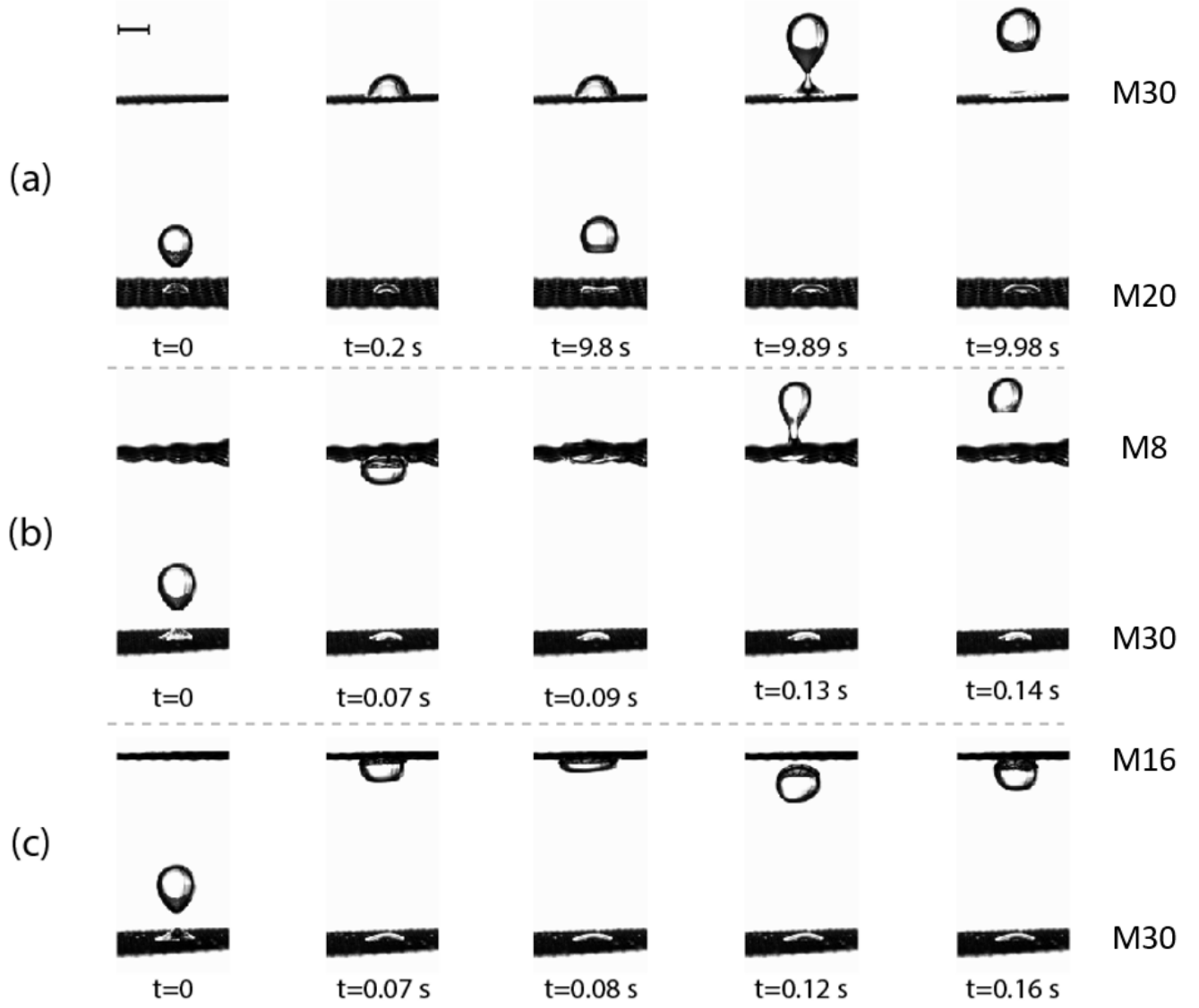


Figure 6: Time-lapsed images showing (a): super-aerophilic mesh M30 ( $w = 0.56$  mm) placed above a super-aerophilic mesh M20 ( $w = 0.86$  mm): the top mesh captures two air bubbles arising from the bottom mesh ( $V \simeq 108 \mu\text{L}$ ) before releasing a larger bubble; (b) super-aerophilic mesh M8 ( $w = 2.46$  mm) on top of a super-aerophilic mesh M30: the top mesh is not able to trap a single bubble rising from the bottom mesh ( $V \simeq 115 \mu\text{L}$ ), and pinch-off occurs after impact of a single bubble; (c) super-aerophobic mesh M16 ( $w = 1.14$  mm) on top of a super-aerophilic mesh M30: the bubble coming from the bottom mesh ( $V \simeq 115 \mu\text{L}$ ) bounces on the bottom surface of the top mesh and remains there. The size of the incoming bubbles in all three cases is  $d_{eq} = 1.86$  mm. The scale bar at top left denotes 5 mm.

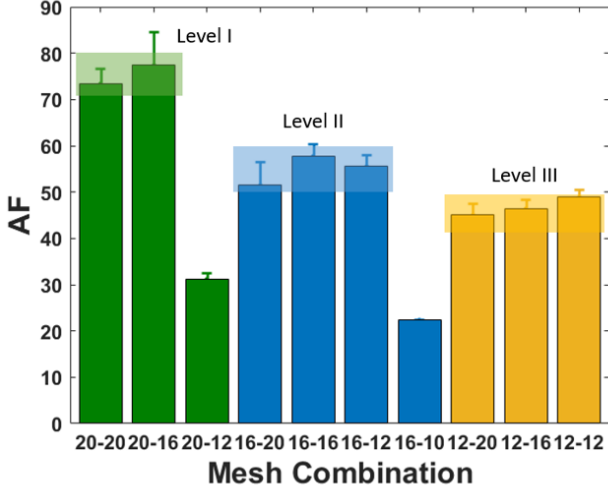


Figure 7: Amplification Factor (AF) resulting from possible combinations of M20 ( $w = 0.86$  mm), M16 ( $w = 1.14$  mm), M12 ( $w = 1.52$  mm), and M10 ( $w = 1.90$  mm) super-aerophilic meshes. The size of the incoming bubbles is  $d_{eq} = 1.86$  mm in all cases.

going bubble from this mesh. The OG bubble volumes for the three different mesh combinations are shown in Fig. 8.  $V_{OG}$  decreases with decreasing pore-size of the top mesh, and accordingly,  $\Delta V_{series}$  rises as the top mesh gets finer. This observation supports the hypothesis that finer meshes can retain a larger amount of air after bubble pinch-off, due to the larger solid-gas interface available there.

## Gas bubbles interacting with wettability-patterned meshes

A wettability pattern is fabricated on both the top and bottom surfaces of the mesh in the manner shown in Fig 1 B5-B7. The perimeter,  $p$ , of the super-aerophilic region, which is responsible for determining  $F_C$ , can be precisely varied by varying the geometry of the pattern. In the uniform-wettability case, the dried perimeter was determined by the spreading capability of air on the mesh, and was affected by the wake effect. An IC bubble rising in water produces a wake, which influences the trajectory of the following bubble.<sup>49,50</sup> This results in small variations in the impact locations, leading to an extended dry perimeter. As

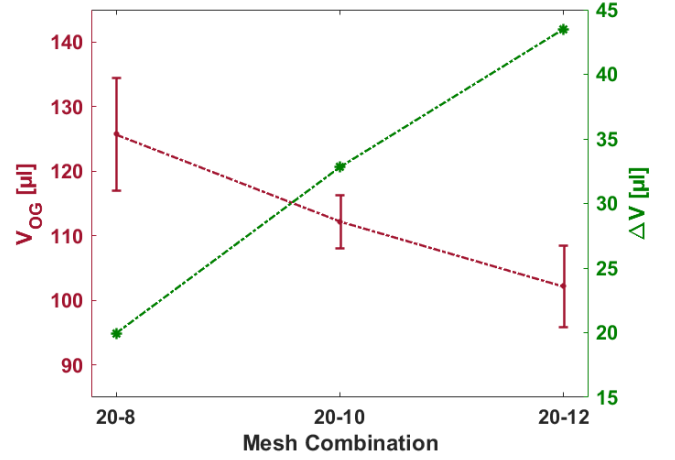


Figure 8: Outgoing bubble volume  $V_{OG}$  resulting from super-aerophilic M8 ( $w = 2.46$  mm), M10 ( $w = 1.90$  mm), and M12 ( $w = 1.52$  mm) super-aerophilic meshes placed above the M20 ( $w = 0.86$  mm) super-aerophilic mesh.  $\Delta V$  is the gas volume left behind in the top mesh after pinch-off of the OG bubble.

previously mentioned, the volume of the outgoing bubbles detaching from the mesh depends on the balance between buoyancy and capillary forces. Therefore, by precisely controlling the dry perimeter, and thus  $F_C$ ,  $V_{OG}$  can be precisely controlled (see Video S4 of the Supporting Information). As shown in Fig. 5a, the  $V_{OG}$  resulting from the impact of a stream of bubbles with  $d_{eq} = 1.86$  mm on a uniformly super-aerophilic M20 mesh was  $108.1 \pm 1.9 \mu\text{L}$ . By forming  $2 \times 2$  and  $3 \times 3$  squares super-aerophilic regions on an otherwise super-aerophobic M20 mesh, the resulting  $V_{OG}$  are, respectively,  $46.30 \pm 1.2 \mu\text{L}$ , and  $89.54 \pm 0.42 \mu\text{L}$ . Therefore, wettability-patterning is useful to produce bubbles having different  $V_{OG}$  from the same mesh. An indicative example of this capability is presented in Fig. 9 for patterned M30 meshes.

Square patterns with three different perimeters were also fabricated on both sides of initially super-aerophobic M20 ( $w = 0.86$  mm) and M30 ( $w = 0.56$  mm) meshes, and the respective  $V_{OG}$  volumes were measured. Naturally, in order for air to spread over the entire super-aerophilic domain on the mesh, the extent of this domain should not be more than the maximum air spreading capability for the same

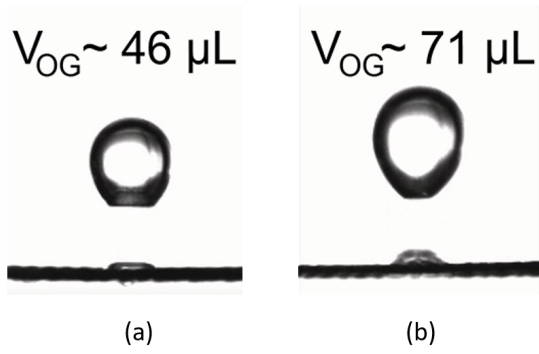


Figure 9: (a) Outgoing bubble volume released from a super-aerophobic M30 mesh ( $w = 0.56 \text{ mm}$ ) patterned with a  $3 \times 3$  grid square super-aerophilic region. (b) Outgoing bubble resulting from a similar super-aerophobic M30 mesh patterned with a  $5 \times 5$  square super-aerophilic region. The size of the incoming bubbles in both cases was  $d_{eq} = 1.86 \text{ mm}$  ( $V_{IC} = 3.37 \mu\text{L}$ ).

uniformly super-aerophilic mesh. The buoyancy force is  $F_B = V_{OG}(\rho_l - \rho_g)g$ , and the capillary force is  $F_C = \sigma p$ , with  $p$  being the perimeter of the super-aerophilic region enforced by the wettability-pattern. As seen from Fig. 10, which plots  $F_B$  vs.  $F_C$ , the relationship between buoyant and capillary forces is linear. Furthermore, since  $F_B \propto V_{OG}$  and  $F_C \propto p$ , it is

$$\frac{\Delta F_B}{\Delta F_C} = \text{const} = k \frac{\Delta V_{OG}}{\Delta p} \quad (5)$$

where  $k = (\rho_l - \rho_g)g/\sigma$ , and  $\Delta$  signifies increment (or decrement). In the case of the M20 mesh,  $\text{const} = 1.15$ , while for the M30 mesh,  $\text{const} = 0.71$ . Therefore, once the  $V_{OG}$  resulting from a given dried perimeter is known, it is possible to predict the  $V_{OG}$  resulting from a defined increment in  $p$ . For a given mesh with perimeter of a single pore  $p^*$ , it is possible to extrapolate the outgoing bubble volume,  $V_{OG}^*$ , resulting from patterning one pore of the mesh.  $V_{OG}^*$  and  $p^*$  can be taken as a reference so that  $\Delta V_{OG} = (V_{OG} - V_{OG}^*)$ , and  $\Delta p = (p - p^*)$ . Figure 10 shows  $F_B$  to be significantly smaller than  $F_C$  at detachment. This may be due to the fact that the volume of the bubble just before detachment (i.e. the volume for which buoyancy is supposed to balance capillarity) differs from  $V_{OG}$  by a quantity  $\Delta V$ , as shown in Fig. 4. Furthermore, the slope of the M20 curve in Fig.

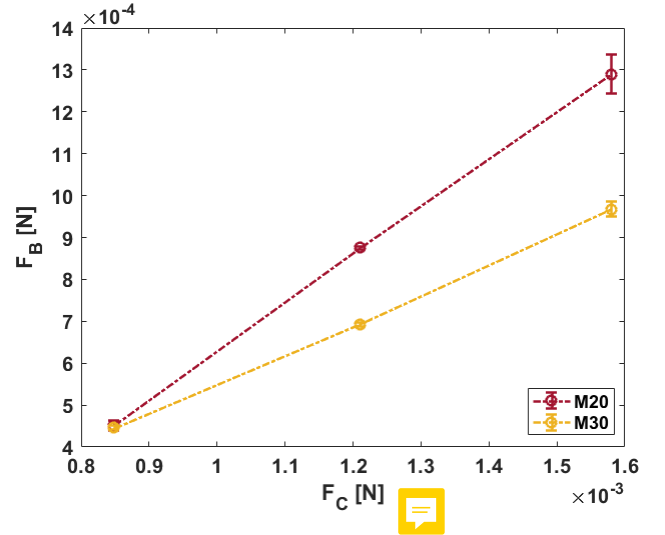


Figure 10: Buoyancy force  $F_B$  plotted against capillary force,  $F_C$ , for dried perimeter ( $p$ ) from 11.8 mm to 21.9 mm. Meshes M20 ( $w = 0.86 \text{ mm}$ ) and M30 ( $w = 0.56 \text{ mm}$ ) were employed, and the size of the incoming bubbles was  $d_{eq} = 1.86 \text{ mm}$  in all cases.

10 is higher than for M30, which indicates that for the same dry perimeter, the bubble released from the M20 mesh would be larger than the M30 mesh. Thus, it can be inferred that the M30 mesh retain a larger fraction of the gas after pinch-off, as compared to the M20 mesh. Consequently, the slope of the straight lines in Fig. 10 is indicative of the capability of the respective mesh to retain air after pinch-off. This retaining capability is quantified here through a dimensionless parameter RC. Since a higher slope of a line in Fig. 10 infers a lower amount of air retained in the mesh, the slope can be assumed to vary as  $1/\text{RC}$ . Therefore, a first-level model for estimating  $V_{OG}$  released from a super-aerophobic mesh patterned with a square super-aerophilic region of perimeter  $p$  can be

$$V_{OG} \simeq \frac{p - p^*}{kRC} + V_{OG}^* \quad (6)$$

This equation can be used to predict  $V_{OG}$  for a mesh with  $p^*$  and patterned with a square super-aerophilic region having perimeter  $p$ , once RC and  $V_{OG}^*$  have been determined experimentally. It is worth noticing that the effective value of  $p$  may slightly differ from the one imposed by the wettability pattern, because of the interwoven nature of the mesh wires at

the junction points. This source of error could be eliminated by using punched meshes instead of woven-wire meshes.

## Conclusions

The possibility of manipulating gas micro-volumes, in the form of buoyantly-rising bubbles, with submerged meshes of controlled wettability has been demonstrated in this work. Super-aerophobic meshes have been shown to prevent or allow the passage of air bubbles depending on the ratio of bubble volume-equivalent diameter to mesh pore size, and bubble-on-mesh impact velocity. Therefore, super-aerophobic meshes may be employed to act as filters that selectively allow passage of gas bubbles depending on their relative size with respect to the mesh openings.

The utility of super-aerophilic meshes for amplifying or reducing the volume of a train of incoming bubbles has also been shown. An amplification factor (AF) has been defined as the ratio of the volume of the outgoing bubble to that of a single incoming bubble. The experiments show that the finer the mesh, the greater the amplification factor. The maximum AF obtained for a single super-aerophilic mesh in the present experiments was about 34.

A further enhancement in AF was obtained by vertically stacking two uniform super-aerophilic meshes held horizontally and separated by a fixed gap. The greatest amplification factor observed in this case was about 78. It was shown that if the pore size of the top mesh is significantly larger than the pore size of the bottom mesh, then the top mesh could not trap the entire amount of air rising from the bottom mesh. The volume of the outgoing bubble from the top mesh is smaller than the volume of the incoming bubble, since a fraction of the incoming air volume is retained in the mesh pores of the top mesh.

In another configuration, a wettability pattern was applied on the top and bottom surfaces of a mesh, so that a super-aerophilic region surrounded by a super-aerophobic domain was obtained. Square-shaped, super-aerophilic regions

were patterned on super-aerophobic meshes, and the perimeter of these regions was varied incrementally. Experiments revealed a linear relationship between the buoyancy force pushing the bubble upwards, and the capillary force holding the bubble attached on the mesh. A gas-retaining capability, RC, was defined to quantify the air volume trapped in the mesh after bubble pinch-off. RC was found to increase with decreasing mesh pore size. Finally, the work produced an analytic expression for the volume  $V_{OG}$  of the outgoing bubble in terms of the dried perimeter of the patterned super-aerophilic domain, the value of RC, the perimeter of a single pore, the properties of the two fluids, and the outgoing bubble volume from a single pore of the same mesh.

## Supporting Information

Video S1, Gas bubble interacting with a super-aerophobic mesh.

Video S2, Gas bubbles interacting with a super-aerophilic mesh.

Video S3, Gas bubbles interacting with a series of parallel super-aerophilic meshes.

Video S4, Gas bubbles interacting with a wettability-patterned mesh.

## Acknowledgements

J.B. conducted this study as part of the TOP-UIC program between Politecnico di Torino and the University of Illinois at Chicago. U.S. acknowledges the financial support from the UIC Graduate College during the course of the present study. The laser marking system of the Nanotechnology Core Facility at UIC was used for sample fabrication, with assistance from Dr. Tamal Roy and Dr. Theodore P. Koukoravas, of the Micro/Nanoscale Fluid Transport Laboratory at UIC. Thanks to Hélène Della Monica of the Micro/Nanoscale Fluid Laboratory at UIC for help in producing the supporting videos.



# References

- (1) Cassie, A. Contact angles. *Faraday Discuss. Chem. Soc.* **1948**, *3*, 11–16.
- (2) Wenzel, R. N. Resistance of solid surfaces to wetting by water. *Ind. Eng. Chem. Res.* **1936**, *28*, 988–994.
- (3) Cassie, A.; Baxter, S. Wettability of porous surfaces. *J. Chem. Soc. Faraday Trans.* **1944**, *40*, 546–551.
- (4) De Gennes, P.-G.; Brochard-Wyart, F.; Quéré, D. *Capillarity and wetting phenomena: drops, bubbles, pearls, waves*; Springer Science & Business Media, 2013; pp 15–181.
- (5) Koch, K.; Barthlott, W. Superhydrophobic and superhydrophilic plant surfaces: an inspiration for biomimetic materials. *Philos. Trans. A Math. Phys. Eng. Sci.* **2009**, *367*, 1487–1509.
- (6) Ma, M.; Hill, R. M. Superhydrophobic surfaces. *Curr. Opin. Colloid Interface Sci.* **2006**, *11*, 193–202.
- (7) Yang, J.; Zhang, Z.; Xu, X.; Men, X.; Zhu, X.; Zhou, X. Superoleophobic textured aluminum surfaces. *New J. Chem.* **2011**, *35*, 2422–2426.
- (8) Zhang, X.; Shi, F.; Niu, J.; Jiang, Y.; Wang, Z. Superhydrophobic surfaces: from structural control to functional application. *J. Mater. Chem.* **2008**, *18*, 621–633.
- (9) Füstner, R.; Barthlott, W.; Neinhuis, C.; Walzel, P. Wetting and self-cleaning properties of artificial superhydrophobic surfaces. *Langmuir* **2005**, *21*, 956–961.
- (10) Marmur, A. Underwater superhydrophobicity: theoretical feasibility. *Langmuir* **2006**, *22*, 1400–1402.
- (11) Bobji, M. S.; Kumar, S. V.; Asthana, A.; Govardhan, R. N. Underwater sustainability of the "Cassie" state of wetting. *Langmuir* **2009**, *25*, 12120–12126.
- (12) McHale, G.; Newton, M. I.; Shirtcliffe, N. J. Immersed superhydrophobic surfaces: Gas exchange, slip and drag reduction properties. *Soft Matter* **2010**, *6*, 714–719.
- (13) Dorrer, C.; Rühe, J. Superaerophobicity: repellence of air bubbles from submerged, surface-engineered silicon substrates. *Langmuir* **2012**, *28*, 14968–14973.
- (14) Zhou, D.; Mi, J.; Zhong, C. Theoretical study of dissolved gas at a hydrophobic interface. *J. Phys. Chem. C* **2012**, *116*, 3042–3049.
- (15) Peng, H.; Birkett, G. R.; Nguyen, A. V. Progress on the Surface Nanobubble Story: What is in the bubble? Why does it exist? *Adv. Colloid Interface Sci.* **2015**, *222*, 573–580.
- (16) Di Mundo, R.; Bottiglione, F.; Palumbo, F.; Notarnicola, M.; Carbone, G. Filamentary superhydrophobic Teflon surfaces: Moderate apparent contact angle but superior air-retaining properties. *J. Colloid Interface Sci.* **2016**, *482*, 175–182.
- (17) Tricinci, O.; Terencio, T.; Mazzolai, B.; Pugno, N. M.; Greco, F.; Mattoli, V. 3D micropatterned surface inspired by salvinia molesta via direct laser lithography. *ACS Appl. Mater. Interfaces* **2015**, *7*, 25560–25567.
- (18) George, J. E.; Chidangil, S.; George, S. D. Recent progress in fabricating superaerophobic and superaerophilic surfaces. *Adv. Mater. Interfaces* **2017**, *4*, 1601088.
- (19) Pei, C.; Peng, Y.; Zhang, Y.; Tian, D.; Liu, K.; Jiang, L. An Integrated Janus Mesh: Underwater Bubble Antibuoyancy Unidirectional Penetration. *ACS nano* **2018**, *12*, 5489–5494.
- (20) Wilkinson, P. M.; Spek, A. P.; van Dierendonck, L. L. Design parameters estimation for scale-up of high-pressure bubble columns. *AIChE J.* **1992**, *38*, 544–554.

- (21) Shah, Y.; Kelkar, B. G.; Godbole, S.; Deckwer, W.-D. Design parameters estimations for bubble column reactors. *AIChE J.* **1982**, *28*, 353–379.
- (22) Mouza, A.; Dalakoglou, G.; Paras, S. Effect of liquid properties on the performance of bubble column reactors with fine pore spargers. *Chem. Eng. Sci.* **2005**, *60*, 1465–1475.
- (23) Kantarci, N.; Borak, F.; Ulgen, K. O. Bubble column reactors. *Process Biochem.* **2005**, *40*, 2263–2283.
- (24) Suzuki, R.; Tanaka, Y.; Arai, K.; Yokota, S. Bubble Elimination in Oil for Fluid Power Systems. *SAE Trans.* **1998**, 381–386.
- (25) Wojke, R. Device for separating gas bubbles from fluids, in particular blood. 1998; US Patent 5,849,065.
- (26) Allen, T. M.; Cullis, P. R. Drug delivery systems: entering the mainstream. *Science* **2004**, *303*, 1818–1822.
- (27) Sen, U.; Chatterjee, S.; Ganguly, R.; Dodge, R.; Yu, L.; Megaridis, C. M. Scaling laws in directional spreading of droplets on wettability-confined diverging tracks. *Langmuir* **2018**, *34*, 1899–1907.
- (28) Clift, R.; Grace, J.; Weber, M. *Bubbles, drops, and particles*; Academic Press, New York, 1978; Vol. 510.
- (29) Amaya-Bower, L.; Lee, T. Single bubble rising dynamics for moderate Reynolds number using Lattice Boltzmann Method. *Comput. Fluids* **2010**, *39*, 1191–1207.
- (30) Hadamard, J. Mouvement permanent lent d’une sphère liquide et visqueuse dans un liquide visqueux. *CR Hebd. Seances Acad. Sci. Paris* **1911**, *152*, 1735–1738.
- (31) Rybczynski, W. On the translatory motion of a fluid sphere in a viscous medium. *Bull. Acad. Sci., Cracow, Ser. A* **1911**, *40*.
- (32) Mendelson, H. D. The prediction of bubble terminal velocities from wave theory. *AIChE J.* **1967**, *13*, 250–253.
- (33) Davies, R.; Taylor, G. I. The mechanics of large bubbles rising through extended liquids and through liquids in tubes. *Proc. R. Soc. Lond. A. Math. Phys. Sci.* **1950**, *200*, 375–390.
- (34) Aybers, N.; Tapucu, A. The motion of gas bubbles rising through stagnant liquid. *Wärme-und Stoffübertragung* **1969**, *2*, 118–128.
- (35) Höller, V.; Wegracht, D.; Kiwi-Minsker, L.; Renken, A. Fibrous structured catalytic beds for three-phase reaction engineering: Hydrodynamics study in staged bubble columns. *Catalysis today* **2000**, *60*, 51–56.
- (36) Jain, D.; Lau, Y. M.; Kuipers, J.; Deen, N. G. Discrete bubble modeling for a micro-structured bubble column. *Chemical Engineering Science* **2013**, *100*, 496–505.
- (37) Baltussen, M.; Kuipers, J.; Deen, N. A numerical study of cutting bubbles with a wire mesh. *Chemical Engineering Science* **2017**, *165*, 25–32.
- (38) Shapiro, A. H. *Compressible fluid flow*; 1953; Vol. 1; pp S2–86.
- (39) Lorenceau, É.; Quéré, D. Drops impacting a sieve. *Journal of colloid and interface science* **2003**, *263*, 244–249.
- (40) Lee, C.; Nam, Y.; Lastakowski, H.; Hur, J. I.; Shin, S.; Biance, A.-L.; Pirat, C.; Ybert, C., et al. Two types of Cassie-to-Wenzel wetting transitions on superhydrophobic surfaces during drop impact. *Soft Matter* **2015**, *11*, 4592–4599.
- (41) Bartolo, D.; Bouamrine, F.; Verneuil, E.; Buguin, A.; Silberzan, P.; Moulinet, S. Bouncing or sticky droplets: Impalement transitions on superhydrophobic micropatterned surfaces. *EPL (Europhysics Letters)* **2006**, *74*, 299.

- (42) Cimadoro, J.; Ribba, L.; Goyanes, S.; Cerda, E. Wetting a superomniphobic porous system. *Soft Matter* **2019**,
- (43) Ma, D.; Liu, M.; Zu, Y.; Tang, C. Two-dimensional volume of fluid simulation studies on single bubble formation and dynamics in bubble columns. *Chemical Engineering Science* **2012**, *72*, 61–77.
- (44) Meehan, R.; Donnelly, B.; Nolan, K.; Persoons, T.; Murray, D. Flow structures and dynamics in the wakes of sliding bubbles. *International Journal of Multiphase Flow* **2016**, *84*, 145–154.
- (45) Zhang, A.; Sun, P.; Ming, F. An SPH modeling of bubble rising and coalescing in three dimensions. *Computer Methods in Applied Mechanics and Engineering* **2015**, *294*, 189–209.
- (46) Liu, Z.; Zheng, Y.; Jia, L.; Zhang, Q. Study of bubble induced flow structure using PIV. *Chemical Engineering Science* **2005**, *60*, 3537–3552.
- (47) Park, R.; Kim, W. Bubble collisions on parallel arranged fibers. *International Journal of Multiphase Flow* **2019**, *118*, 165–172.
- (48) Boscariol, C.; Chandra, S.; Sarker, D.; Crua, C.; Marengo, M. Drop impact onto attached metallic meshes: liquid penetration and spreading. *Experiments in Fluids* **2018**, *59*, 189.
- (49) Bhaga, D.; Weber, M. Bubbles in viscous liquids: shapes, wakes and velocities. *J. Fluid Mech.* **1981**, *105*, 61–85.
- (50) De Vries, A.; Biesheuvel, A.; Van Wijngaarden, L. Notes on the path and wake of a gas bubble rising in pure water. *Int. J. Multiphase Fl.* **2002**, *28*, 1823–1835.